Monthly Notices
of the
ROYAL ASTRONOMICAL SOCIETY

Mon. Not. R. Astron. Soc. **405,** 209–218 (2010) doi:10.1111/j.1365-2966.2010.16476.x

Unresolved X-ray emission in M31 and constraints on progenitors of classical novae

Á. Bogdán[1]★ and M. Gilfanov[1,2]★

[1]*Max-Planck-Institut für Astrophysik, Karl-Schwarzschild-Str.1, 85741 Garching bei München, Germany*
[2]*Space Research Institute, Russian Academy of Sciences, Profsoyuznaya 84/32, 117997 Moscow, Russia*

Accepted 2010 February 3. Received 2010 February 1; in original form 2009 December 23

ABSTRACT

We investigate unresolved X-ray emission from M31 based on an extensive set of archival *XMM–Newton* and *Chandra* data. We show that extended emission, found previously in the bulge and thought to be associated with a large number of faint compact sources, extends to the disc of the galaxy with similar X-ray to *K*-band luminosity ratio. We also detect excess X-ray emission associated with the 10-kpc star-forming ring. The L_X/SFR (star formation rate) ratio in the 0.5–2 keV band ranges from zero to $\approx 1.8 \times 10^{38}$ (erg s^{-1})/(M$_\odot$ yr^{-1}), excluding the regions near the minor axis of the galaxy where it is ∼1.5–2 times higher. The latter is likely associated with warm ionized gas of the galactic wind rather than with the star-forming ring itself. Based on this data, we constrain the nature of classical nova (CN) progenitors. We use the fact that hydrogen-rich material, required to trigger the explosion, accumulates on the white dwarf surface via accretion. Depending on the type of the system, the energy of accretion may be radiated at X-ray energies, thus contributing to the unresolved X-ray emission. Based on the CN rate in the bulge of M31 and its X-ray surface brightness, we show that no more than ∼10 per cent of CNe can be produced in magnetic cataclysmic variables, the upper limit being ∼3 per cent for parameters typical of CN progenitors. In dwarf novae, $\gtrsim$90–95 per cent of the material must be accreted during outbursts, when the emission spectrum is soft, and only a small fraction in quiescent periods, characterized by rather hard spectra.

Key words: white dwarfs – galaxies: individual: M31 – galaxies: stellar content – X-rays: diffuse background – X-rays: galaxies.

1 INTRODUCTION

Similarly to other normal galaxies, X-ray emission from the bulge of the Andromeda galaxy is dominated by accreting compact sources (e.g. Voss & Gilfanov 2007). In addition, there is relatively brighter extended emission, the nature of which was explored in Li & Wang (2007); Bogdán & Gilfanov (2008) (hereafter Paper I) based on an extensive set of *Chandra* observations. In Paper I we revealed the presence of warm ionized interstellar medium (ISM) in the bulge which most likely forms a galactic-scale outflow, and showed that the bulk of unresolved emission is associated with old stellar population, similar to the Galactic ridge X-ray emission in the Milky Way (Revnivtsev et al. 2006; Sazonov et al. 2006). Although these studies led to a much better understanding of X-ray emission from the bulge of M31, the disc of the galaxy could not be investigated in similar detail due to insufficient *Chandra* data coverage of the galaxy. The *XMM–Newton* data, available at the time, also did not provide adequate coverage of the galaxy either, with only the northern part of the disc observed with relatively short exposures (Trudolyubov et al. 2005).

Over the last several years *XMM–Newton* completed a survey of M31, data from which have now become publicly available. The numerous pointings with total exposure time of ∼1.5 Ms give a good coverage of the entire galaxy. With these data it has become possible to study X-ray emission from the disc of the galaxy. In the present paper we concentrate on the unresolved emission component and compare its characteristics in the disc and bulge. We also study the 10-kpc star-forming ring to support our earlier claim that excess unresolved emission is associated with star-forming regions in the galactic disc (Paper I).

Classical nova explosions are caused by thermonuclear runaway on the surface of a white dwarf (WD) in a binary system (Starrfield et al. 1972). In order for the nuclear runaway to start, a certain amount of hydrogen-rich material, $\Delta M \sim 10^{-5}$ M$_\odot$, needs to be accumulated on the WD surface (Fujimoto 1982). This material is supplied by the donor star and is accreted on to the WD. Obviously, there is a direct relation between the frequency of CNe and collective accretion rate in their progenitors. The accretion energy

★E-mail: bogdan@mpa-garching.mpg.de (ÁB); gilfanov@mpa-garching.mpg.de (MG)

is released in the form of electromagnetic radiation, the spectrum of which depends on the type of the progenitor system. In certain types of accreting WDs it peaks in the X-ray band, for example in magnetic systems – polars and intermediate polars. Emission from these systems contributes to the unresolved emission in the galaxy, therefore their number and contribution to the CN rate can be constrained using high-resolution X-ray data. This is the subject of the second part of the paper. Note, that a similar line of arguments can be used to constrain the nature of progenitors of Type Ia supernovae (Gilfanov & Bogdán 2010).

In the following, the distance to M31 is assumed to be 780 kpc (Stanek & Garnavich 1998; Macri 1983) and the Galactic hydrogen column density is 6.7×10^{20} cm^{-2} (Dickey & Lockman 1990).

The paper is structured as follows. In Section 2 we describe the analyzed X-ray and near-infrared data and the main steps in its reduction. In Section 3 results of the analysis of unresolved X-ray emission are presented. In Section 4 we derive constraints on the nature of CN progenitors. Our results are summarized in Section 5.

Table 1. The list of *XMM–Newton* observations used for the analysis.

Obs-ID	$T_{\rm obs}$ (ks)	$T_{\rm filt}$ (ks)	Date
0109270101	62.5	16.0	2001 June 29
0109270301	54.2	25.2	2002 January 26
0109270401	91.6	32.2	2002 June 29
0109270701	54.9	53.7	2002 January 05
0112570101	61.1	52.6	2002 January 06
0112570201	62.8	42.6	2002 January 12
0112570301	59.9	15.2	2002 January 24
0112570401	31.0	25.0	2000 June 25
0202230201	18.3	17.8	2004 July 16
0202230401	14.6	9.0	2004 July 18
0202230501	21.8	2.0	2004 July 19
0402560301	66.7	33.9	2006 July 01
0402560401	57.0	5.0	2006 July 08
0402560501	57.0	24.0	2006 July 20
0402560701	64.4	14.0	2006 July 23
0402560801	64.0	41.0	2006 December 25
0402560901	60.0	33.6	2006 December 26
0402561001	63.6	39.7	2006 December 30
0402561101	60.0	32.0	2007 January 01
0402561301	52.1	25.1	2007 January 03
0402561401	62.0	40.0	2007 January 04
0402561501	54.9	36.9	2007 January 05
0404060201	40.0	14.0	2006 July 03
0410582001	20.1	8.0	2007 July 25

2 DATA REDUCTION

2.1 *XMM–Newton*

We analyzed 24 observations from *XMM–Newton* survey of M31, listed in Table 1. The data were taken between 2000 June 25 and 2007 July 25, and covers nearly the entire disc of M31 and its bulge. The approximate coverage of the galaxy by *XMM–Newton* data is illustrated in the left panel of Fig. 1. We analyzed the data of the European Photon Imaging Camera (EPIC) instruments (Strüder et al. 2001; Turner et al. 2001); for its reduction we used Science Analysis System (SAS) version 7.1.

The main steps of data analysis were performed in the same way as described in Paper I. After applying the double filtering technique (Nevalainen, Markevitch & Lumb 2005), the exposure time decreased to $T_{\rm filt} \approx 639$ ks. The out-of-time (Oot) events were removed using the Oot event list. The exposure maps were calculated with EEXPMAP command of SAS, using a power-law model with slope of $\Gamma = 2$. The observations were re-projected and merged in the coordinate system of Obs-ID 0112570101.

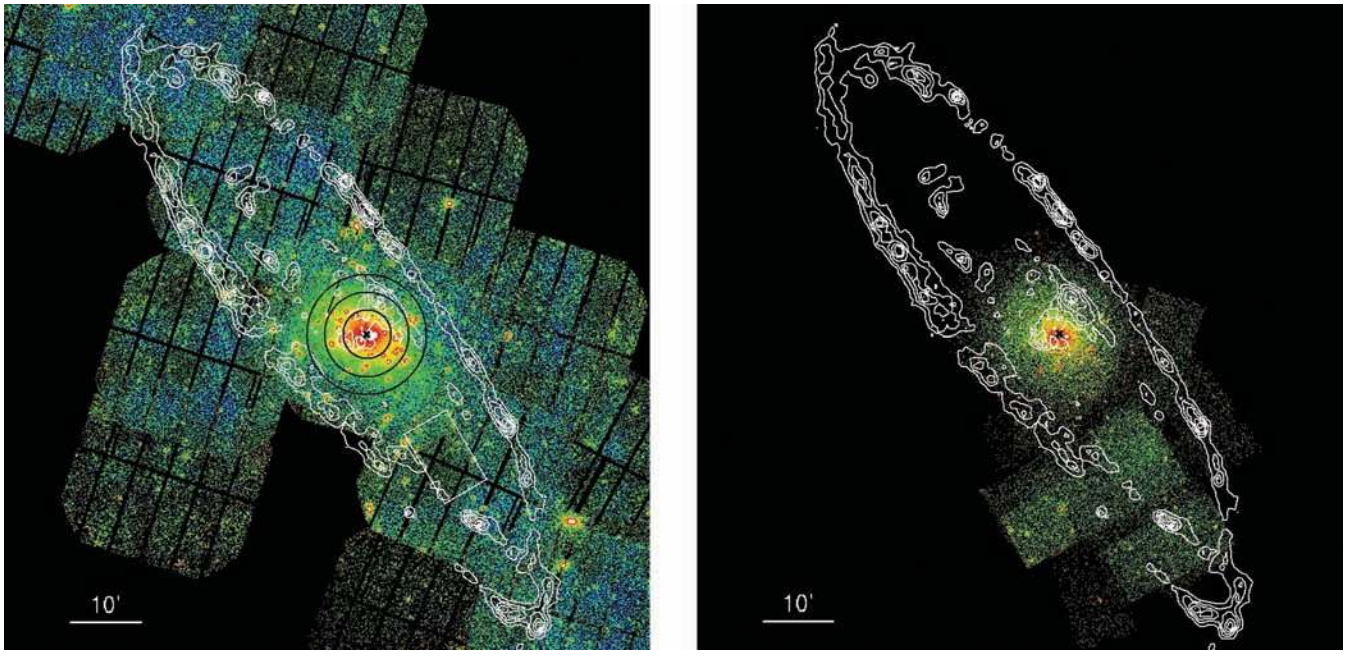

Figure 1. Combined image of *XMM–Newton* (left panel) and *Chandra* (right) observations in the 0.5–2 keV energy band. The instrumental background components are subtracted, and the telescope vignetting correction is applied. White contours show the location of the 10-kpc star-forming ring, traced by the 160 μm *Spitzer* image. Overplotted are the regions used for spectral analysis in Section 3.2 and to compute the $L_{\rm X}/L_K$ ratios in Section 3.3. The centre of M31 is marked with the cross. North is up and east is left.

In the analysis of extended emission, contribution of resolved point sources needs to be removed. For this, we used the *Chandra* source list, where available. In the disc, not covered by *Chandra*, we ran the SAS source detection tool, which gives a complete list of sources above $\sim 10^{36}$ erg s^{-1}. The resulting list was used to mask out compact sources in these regions. As before (Paper I), we use enlarged source regions in order to limit the contribution of remaining counts from point sources to less than $\lesssim$10 per cent.

The particle background components were subtracted as described in Paper I, where their origin is also discussed. By removal of the cosmic X-ray background (CXB) we took into account that the resolved fraction of CXB changes as the exposure time varies. In order to compensate for this effect, we assumed that the point source detection sensitivity is proportional to the exposure time, and computed the resolved fraction of CXB for each pixel using ($\log N - \log S$) distribution from Moretti et al. (2003). We took into account various systematic errors in the background subtraction procedure, which include the scatter in the determination of the 'flat' internal background (caused by the interaction of cosmic rays with the detector material), the uncertainty in the ($\log N - \log S$) distribution, and the uncertainty in the determination of the solar proton component. The combined effect of these uncertainties is indicated by grey shaded area in the surface brightness profiles analyzed in Section 3.1. Due to limitations of the background subtraction procedure, data can be analyzed and interpreted reliably only up to $\sim 1^\circ$ central distance along the major axis of M31 in the 0.5–2 keV energy range. We found that in a harder energy band only the bulge of the galaxy can be studied with *XMM–Newton* data.

2.2 *Chandra*

We combined an extensive set of *Chandra* data taken between 1999 October 13 and 2007 June 2, listed in Table 2. The data were processed with CIAO[1] software package tools (CIAO version 4.0; CALDB version 3.4.5). The 29 observations allowed us to study the bulge and the southern disc of M31, the exact data coverage is shown in the right panel of Fig. 1. In case of ACIS-S observations, we used the data from S1, S2, S3, I2, I3 CCDs, except for Obs-ID 1575 where we extracted data only from the S3 chip. The peak value of the exposure time reaches $T_{\rm filt} \approx 144$ ks in the centre of the galaxy.

The main steps of the data analysis are similar to those outlined in Paper I. After excluding the flare-contaminated time intervals, the total exposure time decreased by $\sim$25 per cent. The instrumental background was subtracted following Hickox & Markevitch (2006) and using the stowed data set.[2] By subtraction of CXB, we followed the same procedure as described for *XMM–Newton*, to correct for the varying fraction of resolved CXB sources.

2.3 Near-infrared data

In order to compare the unresolved X-ray emission with the stellar mass distribution, a stellar mass tracer is needed. The *K*-band image from the Two-Micron All Sky Survey (2MASS) Large Galaxy Atlas (LGA) (Jarrett et al. 2003) image is commonly used for this purpose. Alternatively, one could use data of the Infrared Array Camera (IRAC) on the *Spitzer Space Telescope* (SST), which provides images at near-infrared wavelengths, among others at 3.6 μm.

Due to the large angular extent of M31 the background on the 2MASS *K*-band image provided by LGA is somewhat oversubtracted (T. Jarrett, private communication), therefore the disc of M31 appears to be too faint. In Fig. 2 we compare the *K*-band surface brightness distribution with the *Spitzer* 3.6 μm data. The profiles were extracted along the major axis of M31, with a bin width of 5 arcsec and the bins were averaged on 500 arcsec in the transverse direction. The background level of *Spitzer* image was

Table 2. The list of *Chandra* observations used for the analysis.

Obs-ID	$T_{\rm obs}$ (ks)	$T_{\rm filt}$ (ks)	Instrument	Date
303	12.0	8.2	ACIS-I	1999 October 13
305	4.2	4.0	ACIS-I	1999 December 11
306	4.2	4.1	ACIS-I	1999 December 27
307	4.2	3.1	ACIS-I	2000 January 29
308	4.1	3.7	ACIS-I	2000 February 16
311	5.0	3.9	ACIS-I	2000 July 29
312	4.7	3.8	ACIS-I	2000 August 27
313	6.1	2.6	ACIS-S	2000 September 21
314	5.2	5.0	ACIS-S	2000 October 21
1575	38.2	38.2	ACIS-S	2001 October 05
1577	5.0	4.9	ACIS-I	2001 August 31
1580	5.1	4.8	ACIS-S	2000 November 17
1583	5.0	4.1	ACIS-I	2001 June 10
1585	5.0	4.1	ACIS-I	2001 November 19
2049	14.8	11.6	ACIS-S	2000 November 05
2050	13.2	10.9	ACIS-S	2001 March 08
2051	13.8	12.8	ACIS-S	2001 July 03
2895	4.9	3.2	ACIS-I	2001 December 07
2896	5.0	3.7	ACIS-I	2002 February 06
2897	5.0	4.1	ACIS-I	2002 January 08
2898	5.0	3.2	ACIS-I	2002 June 02
4360	5.0	3.4	ACIS-I	2002 August 11
4536	54.9	30.2	ACIS-S	2005 March 07
4678	4.9	2.7	ACIS-I	2003 November 09
4679	4.8	2.7	ACIS-I	2003 November 26
4680	5.2	3.2	ACIS-I	2003 December 27
4681	5.1	3.3	ACIS-I	2004 January 31
4682	4.9	1.2	ACIS-I	2004 May 23
7064	29.1	23.2	ACIS-I	2006 December 04
7068	9.6	7.7	ACIS-I	2007 June 02

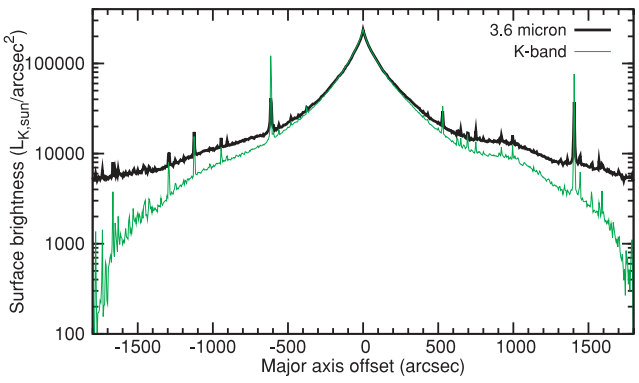

Figure 2. Near-infrared light distribution along the major axis of M31 based on 3.6 μm data of *Spitzer Space Telescope* (black thick line) and the 2MASS *K*-band (thin green line) data. The normalization of *Spitzer* profile was adjusted to match the *K*-band light in the centre of M31. The *x*-coordinate increases from south-west to north-east.

[1] http://cxc.harvard.edu/ciao/
[2] http://cxc.harvard.edu/contrib/maxim/stowed/

estimated using nearby fields to M31. There is a good agreement in the central ∼300 arcsec, where the background subtraction is nearly negligible, but at large offsets an increasing deviation appears. Therefore in the present study we use the 3.6-μm image of *Spitzer* to trace the stellar mass. In order to facilitate the comparison of results with other studies we converted *Spitzer* near-infrared luminosities to *K*-band values using the central regions of the galaxy. The obtained conversion factor between pixel values is $C_K/C_{3.6\,\mu\mathrm{m}} \approx 10.4$.

In Paper I we used 2MASS images to compute *K*-band luminosities and stellar masses of different parts of the galaxy. As the analysis of the Paper I did not extend beyond ≈1000 arcsec from the centre, the underestimated disc brightness on the 2MASS image at large offset angles has not affected our results in any significant or qualitative way. It resulted, however, in small quantitative difference in X/*K* ratios between this paper and Paper I.

3 UNRESOLVED X-RAY EMISSION IN M31

3.1 Surface brightness distribution

We study the brightness distribution of unresolved X-ray emission in M31 in the 0.5–2 and 2–7 keV energy range (Figs 3 and 4, respectively). In all cases profiles were averaged over 500 arcsec in the transverse direction. The contribution of resolved point sources is removed. The profiles are corrected for vignetting; furthermore, all instrumental and sky background components are discounted. We found good agreement at all studied distances between *Chandra* and *XMM–Newton* data. In the inner bulge region, which is most crowded with point sources, we consider only *Chandra* data. X-ray light distributions are compared with the 3.6 μm *Spitzer* data.

The left panel of Fig. 3 presents the surface brightness distribution along the major axis of M31 in the 0.5–2 keV band. The shaded area shows the background subtraction uncertainties (see Section 2.1). The profile confirms the presence of the additional soft emission in the central bulge, which was shown to originate from hot ionized gas (see Paper I). Outside few central bins X-ray flux follows the near-infrared profile – unresolved emission associated with the bulge of the galaxy continues into the disc with approximately the same X-ray to *K*-band ratio. Although the overall correlation between X-ray and near-infrared brightness is quite good, there are several deviations, of which the most prominent is the excess X-ray emission at the central distance of −2500 arcsec. This excess approximately coincides with the broad hump on the 160 μm profile corresponding to the southern end of the 10-kpc star-forming ring (Fig. 1). Similar excess emission ('shoulders' at ∼ ±700 arcsec) coinciding with the peaks on the 160 μm profiles

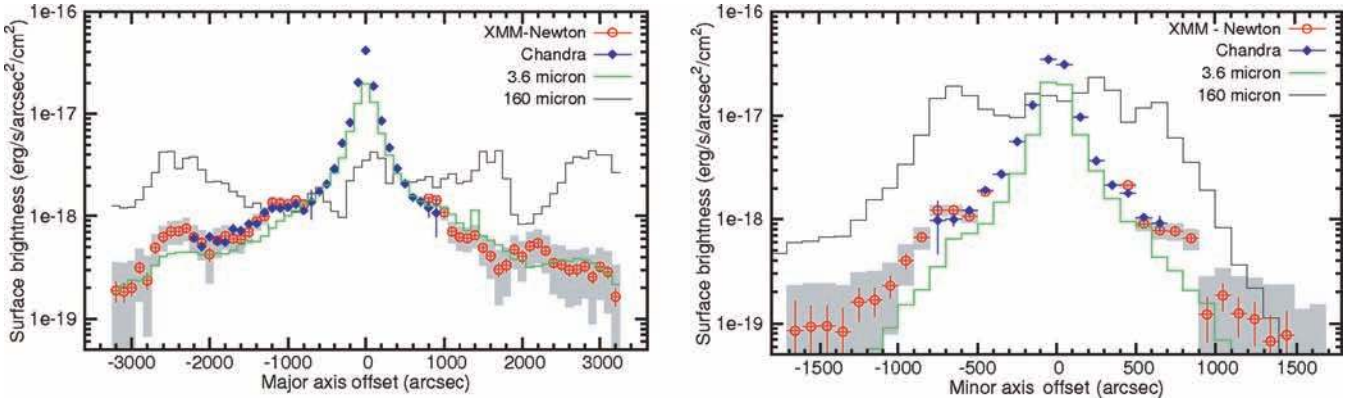

Figure 3. X-ray surface brightness distribution along the major (left panel) and minor axes (right) in the 0.5–2 keV energy band. The filled (blue in the colour version) symbols show the *Chandra* data, open (red) symbols represent the *XMM–Newton* data, the solid (green) histogram is the surface brightness of 3.6 μm *Spitzer* data, the thin solid (black) line is 160 μm *Spitzer* data. The shaded area shows the systematic uncertainty in the background subtraction for the *XMM–Newton* data. The normalization of near- and far-infrared profiles are the same on both panels. The x-coordinate increases from south-west to north-east for the major axis and from south-east to north-west for the minor axis profile.

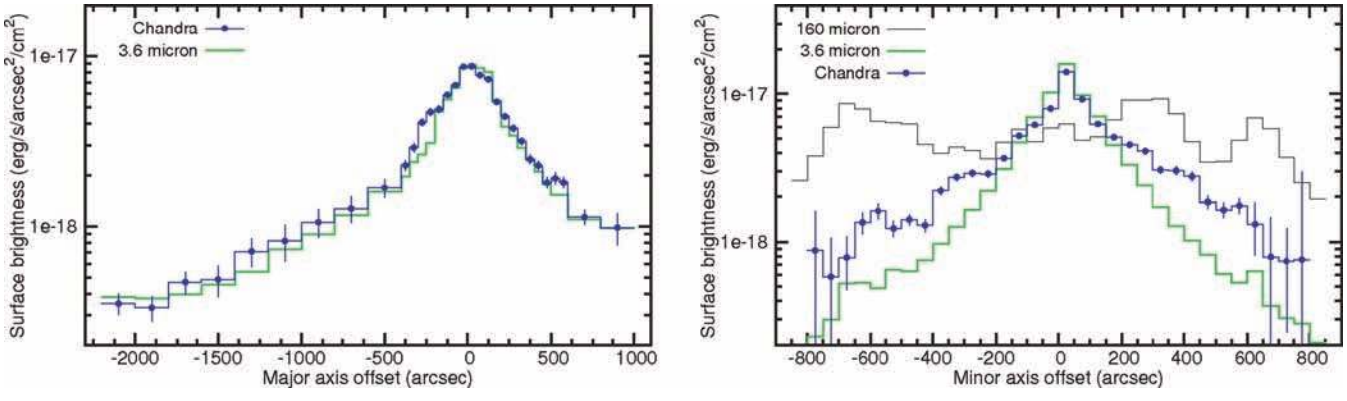

Figure 4. Same as Fig. 3 but in the 2–7 keV energy band, based on *Chandra* data. The normalization of the near-infrared profiles is the same on both panels.

is present in the distribution along the minor axis. (Note that the overall normalization of the X-ray flux is larger on the minor axis profile due to contribution of the gas emission.) A possible association of excess X-ray emission with the star-forming activity in the 10-kpc star-forming ring is further discussed in Section 3.4.

In Fig. 4 we show the brightness distribution in the 2–7 keV energy band based on *Chandra* data. No contribution of the hot gas emission with $kT \sim 300$–400 eV is expected in this energy range. Accordingly, there is a good agreement between the X-ray and near-infrared distribution along the major axis (Fig. 4). However, along the minor axis the unresolved X-ray emission traces the stellar light only in the inner region. Outside ∼200–300 arcsec the X-ray brightness becomes systematically larger than the normalized 3.6 μm distribution. The origin of this enhancement is not clear. It may be associated with the star formation activity in the disc and 10-kpc star-forming ring, as suggested in Paper I, or may be related to the galactic-scale wind.

3.2 Spectra

In order to extract spectra of the bulge and the disc of M31, we used only *Chandra* data. The background was subtracted using the ACIS 'blank-sky' files as described in Paper I. We extracted the spectrum of the inner bulge, outer bulge and disc of M31. The inner bulge region is represented by a circle with 200 arcsec radius, the outer bulge spectrum is extracted from a circular annuli with radii of 350–500 arcsec and the disc spectrum is computed from a rectangular region at the southern part of the disc. The applied regions are also depicted in Fig. 1. As a comparison we also added M32, the extraction region is the same as described in Paper I. In order to compare the spectra, we normalized them to the same level of near-infrared luminosity.

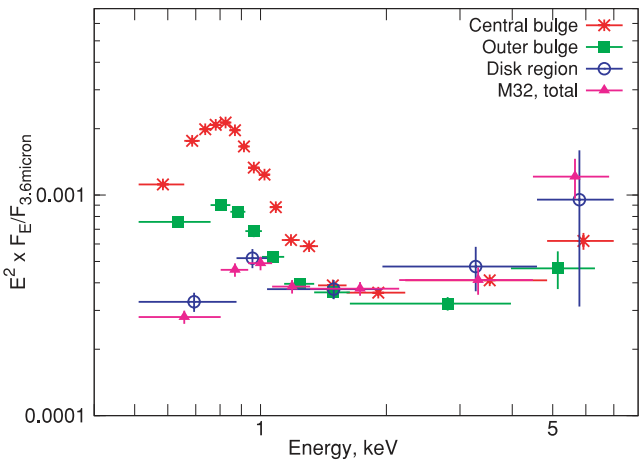

Figure 5. X-ray spectra of different regions in M31 and in M32: stars (red) show the spectrum of the central 200-arcsec region; filled boxes (green) are the spectrum of the 350–500-arcsec annulus; open circles (blue) are the spectrum of the disc; filled triangles (purple) show the spectrum of M32. All spectra were extracted using *Chandra* data. The spectra are normalized to the same level of near-infrared brightness.

Fig. 5 reveals that all spectra are consistent above ∼1.5 keV. Below this energy the inner bulge region is strikingly different: it has a factor of ∼4 times stronger soft component than all other spectra. Also, the outer bulge has a weak excess below ∼1 keV compared to the disc and M32 spectra, which show very similar spectral characteristics at all energies. The remarkable soft component is the consequence of the hot ionized gas, located in the bulge of M31 (see Paper I). The somewhat increased soft emission in the outer bulge is presumably due to the contribution from gas emission, lacking completely in the disc of the galaxy. A relatively weak soft component is also present in the spectra of the disc region and M32, which presumably originates from the population of unresolved sources. Indeed, the different nature of the soft components in the inner bulge and in the disc of M31 is also supported by difference in their best-fitting temperatures. Using a simple two-component spectral model, consisting of an optically thin thermal plasma emission spectrum and a power-law model (MEKAL in XSPEC), we find a best-fitting temperature of $kT = 0.36 \pm 0.01$ keV for the inner bulge, whereas we obtain $kT = 0.62 \pm 0.10$ keV in the disc and $kT = 0.54 \pm 0.15$ keV in M32.

3.3 L_X/L_K ratios

The X-ray to K-band luminosity ratios (L_X/L_K) were computed for the same regions as used for spectral analysis. As before, we use *Chandra* data only. The L_X/L_K ratios are obtained in both 0.5–2 and 2–10 keV energy ranges to facilitate comparison with previous studies. The X-ray luminosities in the 0.5–2 keV energy range were computed using the best-fitting spectral models. For the outer bulge and disc we assumed a 'power law + MEKAL' model, whereas for the inner bulge a second MEKAL component was added to obtain a better fit. In the 2–10 keV band the X-ray luminosities were computed from the count rate using the count-to-erg conversion factor for a power-law spectrum with a photon index of $\Gamma = 2$. The conversion factor depends weakly on the assumed slope, changing by $\lesssim$10 per cent when Γ varied by ±0.4. The luminosities and their ratios are listed in Table 3; errors correspond to statistical uncertainties in the X-ray count rates.

The L_X/L_K ratios for the bulge regions are consistent with those given in Paper I, albeit somewhat smaller, due to the increased K-band luminosity for some of the regions (Section 2.3). In agreement with spectra, the L_X/L_K ratio in the soft band is highest in the inner bulge, and smallest in the disc of the galaxy, where it is consistent with M32 value (Paper I). In the outer bulge the obtained L_X/L_K ratio is in-between due to residual contribution from gas emission. In the hard band all L_X/L_K ratios are similar to each other, in the range of $(3.4$–$4.5) \times 10^{27}$ erg s^{-1} $L_{K,\odot}^{-1}$. There is a statistically significant scatter in their values, origin of which is not clear. It cannot be explained by the varying residual contribution of LMXBs due to

Table 3. X-ray to K-band luminosity ratios for different regions of M31 and for M32.

Region	L_K ($L_{K,\odot}$)	$L_{0.5-2\,kev}$ (erg s^{-1})	$L_{2-10\,kev}$ (erg s^{-1})	$L_{0.5-2\,kev}/L_K$ (erg s^{-1} $L_{K,\odot}^{-1}$)	$L_{2-10\,kev}/L_K$ (ergs^{-1} $L_{K,\odot}^{-1}$)
Inner bulge	$1.9 \cdot 10^{10}$	$1.7 \cdot 10^{38}$	$8.0 \cdot 10^{37}$	$(8.9 \pm 0.1) \cdot 10^{27}$	$(4.2 \pm 0.1) \cdot 10^{27}$
Outer bulge	$8.2 \cdot 10^{9}$	$4.1 \cdot 10^{37}$	$2.9 \cdot 10^{37}$	$(5.0 \pm 0.1) \cdot 10^{27}$	$(3.4 \pm 0.1) \cdot 10^{27}$
Disc	$2.1 \cdot 10^{9}$	$7.6 \cdot 10^{36}$	$9.4 \cdot 10^{36}$	$(3.6 \pm 0.1) \cdot 10^{27}$	$(4.5 \pm 0.2) \cdot 10^{27}$
M32	$8.5 \cdot 10^{8}$	$3.0 \cdot 10^{36}$	$3.4 \cdot 10^{36}$	$(3.5 \pm 0.1) \cdot 10^{36}$	$(4.0 \pm 0.2) \cdot 10^{36}$

different point source detection sensitivities in different regions. Indeed, the latter varies from $\sim 2 \times 10^{35}$ erg s^{-1} in the outer bulge to $\sim 6 \times 10^{35}$ erg s^{-1} in the disc. If we use the luminosity function of LMXBs of Gilfanov (2004) and assume a power-law spectrum with slope of $\Gamma = 1.56$ as average LMXB spectrum (Irwin, Athney & Bregman 2003), we find that LMXBs in the luminosity range of (2–6) $\times 10^{35}$ erg s^{-1} contribute $L_X/L_K \sim 3 \times 10^{26}$ ergs^{-1} L$^{-1}_{K,\odot}$, which may account only for about one-fourth of the scatter. Further contribution to the observed difference in L_X/L_K ratios may be made by the difference in star formation history of different regions. This may be an interesting topic on its own, but it is beyond the scope of this paper.

3.4 Emission from the 10-kpc star-forming ring

Surface brightness profiles suggest that there may be additional emission components associated with spiral arms and the 10-kpc star-forming ring. In order to study this further, we consider X-ray emission along the 10-kpc star-forming ring of the galaxy and investigate the behaviour of the L_X/SFR (star formation rate) ratio. We use *XMM–Newton* data since only they provide a good coverage of the star-forming ring with adequate sensitivity. Due to uncertainties in the background subtraction procedure in the hard energy band, we restrict this study to the 0.5–2 keV range. The X-ray luminosity was computed in the same way as described in Section 3.1. The contribution of unresolved emission associated with old stellar population was removed based on the near-infrared luminosity of studied regions and using the L_X/L_K ratio of the disc of M31. The remaining X-ray emission is 25–50 per cent of of the original value. The SFR was determined based on 160 μm image of the galaxy provided by *Spitzer*. The background level for the latter was determined from a combination of nearby blank sky fields. The SFR was computed from the 160 μm flux using the infrared spectral fits from Gordon et al. (2006) and calibration of Kennicutt (1998). This resulted to a conversion coefficient of SFR $= 9.5 \cdot 10^{-5}$ F$_{160\,\mu m}$/Jy M$_\odot$ yr^{-1} for the distance of M31.

The behaviour of X/SFR ratio along the 10-kpc star-forming ring is shown in Fig. 6. It is the largest in the bins centred at the position angle of ≈90° and ≈270° corresponding to the minor axis of the galaxy. These bins are contaminated by the gas emission as it is obvious from the minor axis soft band profile shown in Fig. 3. On the other hand, no excess X-ray emission above the level corresponding to the L_X/L_K ratio for the disc was detected in the northern (the position angle of ∼10°) and southern (∼215°) parts of the ring. In order to indicate the level of possible systematic uncertainties (the statistical errors are much smaller), we show the level corresponding to 20 per cent of X-ray emission associated with the old stellar population by upper limit signs. Apart from these bins, Fig. 6 clearly demonstrates presence of the excess unresolved emission approximately correlated with the far-infrared luminosity with X/SFR values in the range of (0.9–1.8) $\times 10^{38}$ (erg s^{-1})/(M$_\odot$ yr^{-1}). This emission presumably arises from a multitude of unresolved sources associated with star formation, such as young stellar objects (protostars and pre-main-sequence stars), young stars (e.g. Koyama et al. 1996), low-luminosity Be X-ray binaries. Contribution of supernova remnants and hot X-ray emitting gas may also play a role. The origin of observed variations in the X/SFR ratio is not entirely clear. They may be intrinsic, due to the different star formation history and population age in different parts of the 10-kpc star-forming ring (Shtykovskiy & Gilfanov 2007), or may be caused by varying column density which can be as large as few times 10^{21} cm^{-2} (Nieten et al. 2006). The latter possibility may play particular role in disappearing of the X-ray emission at the position angles of ∼10° and ∼215°. Data in the hard band, unaffected by absorption, could discriminate between these two possibilities. To this end, extensive *Chandra* observations of the 10-kpc star-forming ring would be instrumental.

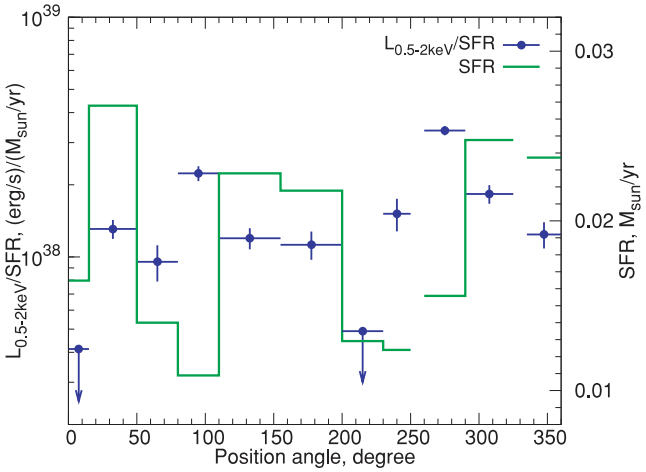

Figure 6. The X/SFR ratio along the 10-kpc star-forming (filled circles with error bars). The position angle increases clockwise and its zero point is at the northern side of the galaxy along its major axis. The bins centred at ≈90° and ≈270° approximately correspond to the minor axis of the galaxy. The solid histogram shows the star formation rate in the same regions (right-hand *y*-axis). No X-ray emission above the level defined by the X/K luminosity ratio of the disc was detected in the bins located at ≈10° and ≈215°. In order to illustrate the amplitude of possible systematic uncertainties, we show by upper limit signs the level, corresponding to 20 per cent of the emission from old population. No X-ray data with sufficient exposure time was available at position angles of ≈250° and ≈330°.

4 PROGENITORS OF CLASSICAL NOVAE IN M31

4.1 X-ray emission from progenitors of classical novae

Classical novae (CNe) are nuclear explosions occurring upon accumulation of critical mass of hydrogen-rich material on the surface of an accreting white dwarf. The frequency of these events in a galaxy depends on the rate at which matter accretes on to white dwarfs, hence it can be related to their luminosity. Indeed, the accretion energy (bolometric) released between two successive CN outbursts is

$$\Delta E_{\rm accr} = \frac{G M_{\rm WD} \Delta M}{R_{\rm WD}}, \qquad (1)$$

where $\Delta M(M_{\rm WD}, \dot{M})$ is the mass of hydrogen-rich material needed to trigger a CN explosion (Yaron et al. 2005) and $M_{\rm WD}$ and $R_{\rm WD}$ are the mass and radius of the white dwarf. For parameters believed to be typical of CN progenitors ($M_{\rm WD} = 1$ M$_\odot$ and $\dot{M} = 10^{-9}$ M$_\odot$ yr^{-1})$\Delta M \approx 4.7 \times 10^{-5}$ M$_\odot$ and total accretion energy released by an accreting WD between two CN explosions is $\Delta E_{\rm accr} \sim 2 \times 10^{46}$ erg. If the frequency of CN events in a galaxy is $\nu_{\rm CN}$, the total accretion luminosity due to CN progenitors is

$$L_{\rm accr} = \Delta E_{\rm accr} \times \nu_{\rm CN}. \qquad (2)$$

Dependence of the accretion luminosity on the mass of the WD and accretion rate is shown in Fig. 7. In computing this curve we used the WD mass–radius relation of Panei, Althaus & Benvenuto (2000)

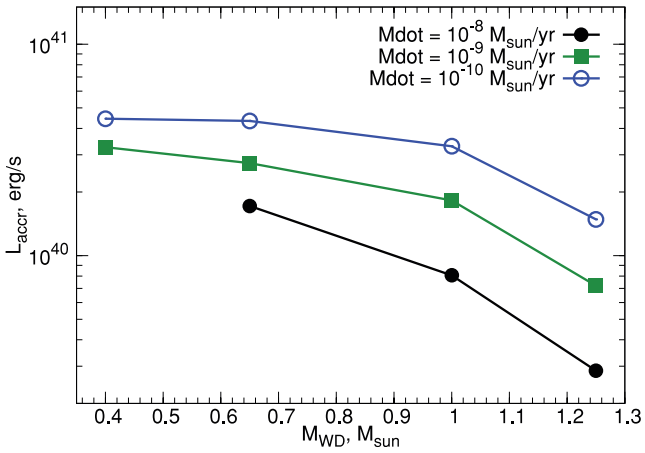

Figure 7. The bolometric luminosity of accreting WDs – progenitors of Classical Novae in a galaxy with CN rate of $\nu_{\rm CN} = 25$ per year. The curves show dependence of $L_{\rm accr}$ on the WD mass for several values of the mass accretion rate.

for a zero-temperature carbon white dwarf and $\Delta M(M_{\rm WD},\ \dot{M})$ dependence from Yaron et al. (2005).

The energy of accretion is radiated in the optical, ultraviolet or X-ray band, depending on the type of the progenitor system. In magnetic systems (polars and intermediate polars) and dwarf novae in quiescence, it is emitted predominantly in the X-ray band. Moreover, their X-ray spectra are relatively hard and their emission is therefore essentially unaffected by the interstellar absorption. X-ray radiation from these objects will contribute to unresolved emission from a galaxy. Therefore, comparing theoretical predictions with the surface brightness of unresolved emission, one can constrain their contribution to the observed CN rate in galaxies. Derivation of such upper limits based on M31 data is the goal of this section.

4.2 Classical novae, resolved X-ray sources and unresolved emission in the bulge of M31

The CN frequency in the bulge of M31 is 25 ± 4 (Shafter & Irby 2001) (see also Arp 1956). The number of progenitors required to maintain this rate is

$$N \sim \frac{\Delta M}{\dot{M}} \nu_{\rm CN}.$$

Typical CN progenitors have accretion rate in the range of $\sim 10^{-10}$–$10^{-8}\,{\rm M}_\odot\,{\rm yr}^{-1}$ (Puebla, Diaz & Hubeny 2007) and WD masses of 0.65–1 $\rm M_\odot$ (Ritter & Kolb 2003). Correspondingly, the number of CN progenitors is in the range of $\sim 2 \times 10^3$–2×10^6, where the smaller number corresponds to the more massive white dwarfs and larger accretion rates. This exceeds significantly the number of bright resolved sources in the bulge of M31, ~300. The latter is dominated by low-mass X-ray binaries – these being excluded, the number of potential bright CN progenitors is yet smaller. We therefore conclude that the majority of CN progenitors cannot be among bright point sources; rather, they are a part of the unresolved X-ray emission.

To measure the latter, we define the bulge as an elliptical region with 12 arcmin major axis, with axis ratio of 0.47 and with position angle of 45°. The total K-band luminosity of the studied region is $L_K = 4.2 \times 10^{10}\,{\rm L}_\odot$. We use *Chandra* data, described in the previous sections, to obtain the unresolved X-ray luminosity in the 2–10 keV energy range. The advantage of this energy band is that it is not polluted by hot ionized gas (Section 3.2). We find a total luminosity of the unresolved component of $L_{2-10\,{\rm keV}} = (1.6 \pm 0.1) \times 10^{38}$ erg s^{-1} in this region. Obviously, this value presents only an upper limit on the luminosity from the population of accreting white dwarfs, as other type of X-ray emitting sources may also contribute. To this end we use results of Sazonov et al. (2006), who studied the population of faint X-ray sources in the Solar neighbourhood and found that accreting WDs contribute about one-third of the total luminosity in the 2–10 keV band. As M31 demonstrates similar X/K ratio, we extrapolate this result to the bulge of M31 and estimate the luminosity of CVs of $L_{\rm CV,2-10\,keV} = (5.7 \pm 0.3) \times 10^{37}$ erg s^{-1}.

4.3 Magnetic cataclysmic variables

4.3.1 Upper limit on the contribution of magnetic systems to the CN rate

Polars (AM Her systems) and intermediate polars (IPs) are accreting binary systems in which the accretion disc is partly (IPs) or entirely (AM Her systems) disrupted by magnetic field of the white dwarf. These systems are sources of relatively hard X-ray emission produced via optically thin bremsstrahlung in an accretion shock near the WD surface. They may also have a prominent soft component generated by the WD surface illuminated by hard X-rays. Theory predicts (Lamb & Masters 1979; King & Lasota 1979) and observations confirm (Ramsay & Cropper 2004) that the soft component account for about half of the total accretion luminosity of polars. Intermediate polars may also have a soft component in their spectra of somewhat smaller luminosity, about one-third of the total (Evans & Hellier 2007). Correspondingly, we assume in the following calculations, that half of the accretion luminosity of magnetic CVs is emitted in the hard X-ray component. To the first approximation, the bremsstrahlung temperature of this component is defined by the depth of the gravitational component on the WD surface, the observed values showing considerable dispersion. For a large sample of magnetic WDs (Landi et al. 2009; Brunschweiger et al. 2009) we calculate the average value of $kT \approx 23$ keV with the standard deviation of ≈9 keV. In the following calculations, we assume $kT = 23$ keV and ignore the dependence of the temperature on the WD mass. As demonstrated below, this particular choice does not influence our results significantly.

In order to constrain the contribution of magnetic CVs to the CN frequency, we compute their predicted X-ray luminosity assuming that CNe are exclusively produced in such systems. In this calculation we assume that the presence of strong magnetic fields does not influence the characteristics of nuclear burning and results of Yaron et al. (2005) for the mass of the hydrogen layer $\Delta M(\dot{M}, M_{\rm WD})$ apply. In particular, we used the $\Delta M(\dot{M}, M_{\rm WD})$ values for the WD temperature of $T_{\rm WD} = 10^7$ K (Townsley & Bildsten 2004). The total accretion luminosity predicted by equation (2) is halved (see above), corrected for interstellar absorption and converted into the 2–10 keV energy band. The obtained value is then compared with the observed luminosity of the unresolved emission, corrected for the contribution of accreting WDs, as described before. The upper limit on the contribution of magnetic systems in the CN rate in M31 is shown in Fig. 8. It shows that allowing all possible values of the WD mass, no more than ≈10 per cent of CNe can be produced in magnetic systems. The less constraining value of the upper limit corresponds to the largest accretion rate and most massive WDs. However, the combination of these extreme parameters is not typical of magnetic CVs as illustrated by the cumulative distribution of the WD mass in magnetic systems (Ritter & Kolb 2003; Suleimanov,

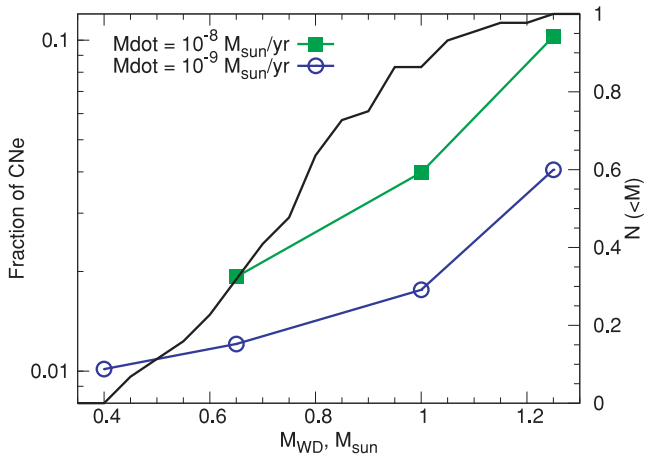

Figure 8. The upper limit of the contribution of magnetic systems to the CN frequency. The filled squares (green in the colour version of this plot) correspond to an accretion rate of 10^{-8} $M_\odot$ yr^{-1}, while the empty circles (blue) assumes an accretion rate of 10^{-9} $M_\odot$ yr^{-1}. The solid line (black) shows the cumulative distribution of white dwarf masses in magnetic CVs (right-hand *y*-axis), see text for references. Note, that 85 per cent of white dwarfs are less massive than 1 $M_\odot$.

Revnivtsev & Ritter 2005; Brunschweiger et al. 2009). The distribution shows that ≈85 per cent of white dwarfs are less massive than 1 $M_\odot$. Furthermore, the average accretion rate in these systems is fairly low, $\dot{M} \sim 1.8 \times 10^{-9}$ $M_\odot$ yr^{-1} (Suleimanov et al. 2005). We conclude therefore that a more realistic upper limit should be ≈3 per cent, corresponding to $M_{\rm WD} = 1$ $M_\odot$ and $\dot{M} = 10^{-9}$ $M_\odot$ yr^{-1}.

This result weakly depends on the assumed temperature of bremsstrahlung spectrum. If $kT = 40$ keV is assumed, the upper limit becomes ≈4 per cent. Only an unrealistically large temperature of $kT = 75$ keV would lead to a two times larger upper limit.

4.3.2 Comparison with statistics of observed CNe from magnetic systems

Ritter & Kolb (2003) find that about one-third of CNe, with known progenitors, are produced in CVs possessing a magnetic white dwarf (Table 4). Although this catalogue is complete neither in the volume nor in the brightness limited sense, the ∼10 times discrepancy appears to be too large to be consistent with our upper limit of ≈3 per cent. In another study, Araujo-Betancor (2005) investigated the space density of magnetic and non-magnetic CVs, and obtained that ∼22 per cent of all CVs are magnetic. This number also seems to be in conflict with our upper limits. As demonstrated below, these two discrepancies are caused by the single reason – by an order of magnitude difference in mass accretion rate between magnetic and non-magnetic system.

Indeed, the average accretion rate in magnetic CVs is $\sim 1.8 \times 10^{-9}$ $M_\odot$ yr^{-1} (Suleimanov et al. 2005), whereas for non-magnetic CNe it is $\sim 1.3 \times 10^{-8}$ $M_\odot$ yr^{-1} (Puebla et al. 2007). The obvious consequence of this difference is that in magnetic systems it takes longer to accrete the same amount of material needed to trigger the nova explosion. Moreover, at lower accretion rates ΔM is larger by a factor of ∼1.5–2 (Yaron et al. 2005). The consequence of these effects is that magnetic CVs undergo CN outburst ∼10–20 times less frequently. This explains the second discrepancy – between the observed fraction of magnetic CVs and our upper limit on their contribution to the CN frequency.

Table 4. The list of magnetic and non-magnetic Galactic CNe, classification is taken from Ritter & Kolb (2003) unless otherwise noted.

Name	CV classification	Distance, pc
V603 Aql	SH	400[b]
V1425 Aql	NL	2700[c]
OY Ara	SW	1500[b]
RS Car	SH	2100[b]
V842 Cen	NL	500[b]
RR Cha	SH	6100[b]
V1500 Cyg	AM[a]	1300[b]
V1974 Cyg	SH	1700[b]
V2275 Cyg	IP	5500[d]
V2467 Cyg	NL	3100[e]
DM Gem	SW	4700[b]
DQ Her	DQ	525[f]
V446 Her	DN	1300[b]
V533 Her	DQ	1300[b]
DK Lac	VY	3900[b]
BT Mon	SW	1000[b]
GI Mon	IP	4600[b]
GQ Mus	AM	5100[b]
GK Per	DN	500[b]
V Per	NL	1000[b]
RR Pic	SW	500[b]
CP Pup	SH	900[b]
HZ Pup	NL	5800[b]
V597 Pup	IP[a]	10 300[g]
T Pyx	SS	2500[b]
V697 Sco	IP	16 100[b]
V373 Sct	IP	4600[b]
WY Sge	DN	2000[b]
V630 Sgr	SH	600[b]
V1017 Sgr	DN	2600[b]
V4633 Sgr	AM[a]	9000[h]
V4745 Sgr	IP	14 000[i]

[a] The classification for V1500 Cyg, V597 Pup and V4633 Sgr was taken from Stockman, Schmidt & Lamb (1988) Warner & Woudt (2009) and Lipkin et al. (2001), respectively.
References are from: [b]Shafter (1997) – [c]Kamath et al. (1997) – [d]Kiss et al. (2002) – [e]Poggiani (2009) – [f]Vaytet, O'Brien & Rushton (2007) – [g]Naik, Banerjee & Ashok (2009) – [h]Lipkin et al. (2001) – [i]Csák et al. (2005)

Another consequence of the smaller accretion rate is that CN explosions are brighter in magnetic systems, therefore they can be observed at larger distances and are sampled from larger volume than CNe from non-magnetic progenitors. This explains the first discrepancy – seemingly too large fraction of CN events, progenitors of which are magnetic systems. To verify this, we selected CNe with known progenitors from the catalogue of Ritter & Kolb (2003) and searched for distances in the literature. In total, we collected 32 CNe, of which 11 are from magnetic progenitors (Table 4). Their distance distributions are shown in Fig. 9. Obviously, magnetic systems are located at larger distances: the average distance is ≈6.6 and ≈2.2 kpc for magnetic and non-magnetic CNe, respectively. Below 1 kpc almost four times more non-magnetic CNe are observed (the normalized number of magnetic systems is ≈1.9 and 8 for non-magnetic), whereas above ≈5 kpc there are more magnetic CVs (≈11.4 versus 3). The difference between two distributions is statistically significant, with the K–S probability of ≈0.008.

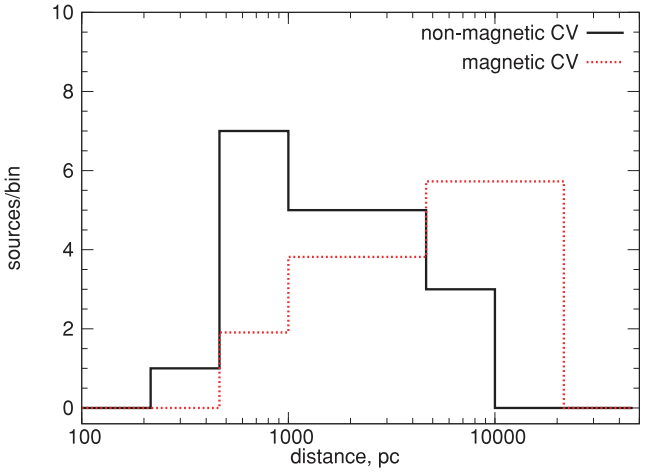

Figure 9. The distance distribution for CNe arising from magnetic and non-magnetic CVs. The total number of magnetic systems is normalized by 1.9 to match the number of non-magnetic ones. The data, used to produce this plot, is given in Table 4.

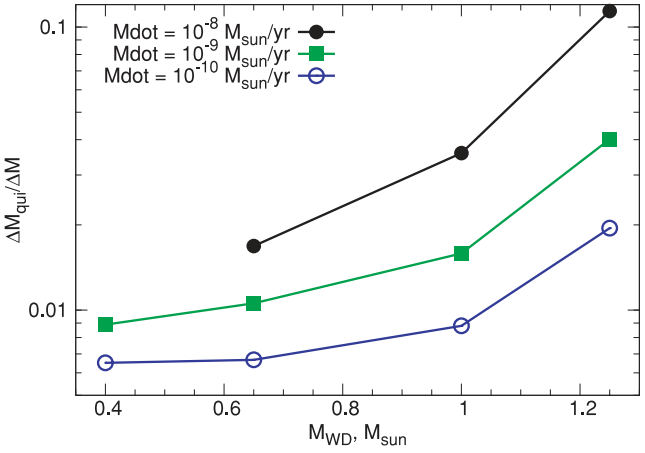

Figure 10. The fraction of mass accreted in quiescence as a function of white dwarf mass. Different mass accretion rates were assumed, the filled circles (black) correspond to 10^{-8} $M_\odot$ yr^{-1}, the filled boxes (green) represent 10^{-9} $M_\odot$ yr^{-1}, whereas the empty circles (blue) stand for 10^{-10} $M_\odot$ yr^{-1}.

The difference in the distance can be compared with the prediction based on the expected brightness at the maximum of the light curve. Calculations of Yaron et al. (2005) show that for 0.65 $M_\odot$ WD, the maximum brightness achieved during the CN explosion will differ by ≈1 mag, the difference being smaller for a more massive WD. Taken at the face value, this would suggest a distance difference of ∼1.6, which is smaller than the observed difference in average distance by a factor of ∼3. Given the crudeness of this calculation, we conclude that these two numbers are broadly consistent with each other.

4.4 Dwarf novae

Dwarf novae (DNe) are a subclass of CVs showing frequent quasi-periodic outbursts due to thermal-viscous instability of the accretion disc (Osaki 1974; Hoshi 1979). In quiescence they become sources of relatively hard X-ray emission from the optically thin boundary layer, whereas in outburst state the optically thick accretion disc emits predominantly in the ultraviolet and soft X-ray bands. One of the models used to describe the emission spectra in quiescence states is a cooling flow model (e.g. Mukai et al. 2003). Spectral analysis of a large number of quiescence spectra showed a relatively large dispersion in the value of the initial temperature $kT_{\rm max} \sim 8$–55 keV with the average value being 23 keV (Pandel et al. 2005). This value is assumed in the calculations performed in this section. It is also assumed that only half of the accretion energy is emitted in the boundary layer.

Dwarf novae give rise to CNe. On the other hand, in the quiescence state they may contribute to the unresolved emission. In the outburst state, to the opposite, soft emission is largely hidden because of the interstellar absorption. Therefore, the bimodal spectral behaviour of dwarf novae can be used to constrain the fraction of mass which is accreted in quiescence, similar to how the upper limit on the contribution of magnetic systems was obtained. Using the same approach, we calculate the X-ray luminosity in the quiescence state assuming that dwarf novae are responsible for about half of the CN events [the other half is due to nova-like variables; Ritter & Kolb (2003)]. With this value one can put an upper limit on the fraction of mass, accreted during quiescence. The result of this calculation is shown in Fig. 10. As in the case of magnetic systems, the absolute upper limit is ∼10 per cent. However, the WD mass in DNe typically does not exceed ≈0.9 $M_\odot$ and the mass accretion rate is not much larger than ≈10^{-8} $M_\odot$ yr^{-1}, therefore the realistic upper limit is ≈3 per cent. As before, this result is not strongly sensitive to the choice of the $kT_{\rm max}$ parameter of the cooling flow model. Assuming $kT_{\rm max} = 55$ keV, our upper limits would increase by ≈1/7 of their value.

Using this upper limit, the enhancement factor of the accretion rate in outburst state can be inferred. Obviously, this quantity depends on the fraction of time spent in the outburst. Since for majority of DNe it is smaller than ∼1/5 (Wils et al. 2009), the accretion rate increases by ∼30–1000 during outburst. This conclusion is consistent with observations of dwarf novae. Indeed, one of the best studied dwarf novae, SS Cyg, spends ∼75 per cent of the time in quiescence (Cannizzo & Mattei 1992). The accretion rate varies from 5×10^{-11} $M_\odot$ yr^{-1} in quiescence (Urban & Sion 2006) to 3.2×10^{-9} $M_\odot$ yr^{-1} in outburst (Hamilton et al. 2007), hence the enhancement factor is 64 and ≈95 per cent of the material is accreted in outburst periods, in good agreement with our results.

4.5 Generalization of the results

Although we considered only the bulge of M31, our results can be generalized to other early-type galaxies.

The X-ray to K-band luminosity ratio in early-type galaxies, galaxy bulges and in the Milky Way is in good agreement in the 2–10 keV band (Revnivtsev et al. 2006; Sazonov et al. 2006; Revnivtsev et al. 2007). On the other hand, for a sample of early-type galaxies, including M31, Williams & Shafter (2004) obtained fairly uniform values of the luminosity-specific nova rate (ν_K), in the range of $(1.8–2.7) \times 10^{-10}$ $L_{\odot,K}$ yr^{-1}. In apparent contradiction with this, we obtain $\nu_K = (6.0 \pm 1.0) \times 10^{-10}$ $L_{\odot,K}$ yr^{-1} for the bulge of M31, based on its CN frequency and K-band luminosity. However, Williams & Shafter (2004) computed the K-band luminosity from (B–K) colour and B-band luminosity of the galaxy, which in case of M31 results in a K-band luminosity larger by a factor of ∼3 than the 2MASS value, and larger by a factor of ∼2 than that deduced from the *Spitzer* data (Williams & Shafter 2004). With this correction, our value for the K-band-specific CN rate for the bulge of M31 corresponds to $\nu_K = (3.0 \pm 0.5) \times 10^{-10}$ $L_{\odot,K}$ yr^{-1}, which is in a good agreement with other galaxies.

As both X/K ratio and ν_K are similar, our conclusions hold for other early-type galaxies as well.

5 CONCLUSION

We studied unresolved X-ray emission from the bulge and disc of M31 using publicly available *XMM–Newton* and *Chandra* data. The *XMM–Newton* survey of M31 covered the entire galaxy with the total exposure time of ≈639 ks after filtering. *Chandra* data covered the bulge and the southern part of the disc, with the exposure time of the filtered data of ≈222 ks.

We demonstrated that unresolved X-ray emission, associated with the bulge of the galaxy, extends into the disc with similar X-ray to K-band luminosity ratio. We obtained $L_{\rm X}/L_K = (3.4\text{–}4.5) \times 10^{27}{\rm ergs}^{-1}\,{\rm L}_{\odot}^{-1}$ in the 2–10 keV band for all studied regions in the bulge and the disc of M31, which is in good agreement with those obtained for the Milky Way and for M32. This suggests that the unresolved X-ray emission in M31 may have an origin similar to the Galactic ridge X-ray emission, namely it is a superposition of a large number of faint compact sources, such as accreting white dwarfs and coronally active binaries.

We investigated X-ray emission associated with the 10-kpc star-forming ring based on *XMM–Newton* data. We characterized this emission with $L_{\rm X}$/SFR ratio, where $L_{\rm X}$ is calculated for the 0.5–2 keV energy range. We found that its value is spatially variable. After excluding the two regions along the minor axis of the galaxy, which are likely contaminated by the hot gas outflow, we obtained values ranging from zero to $L_{\rm X}/{\rm SFR} = 1.8 \times 10^{38}\ ({\rm ergs}^{-1})/(M_{\odot}\ {\rm yr}^{-1})$. The origin of these variations remains unclear.

We derived constraints on the nature of CN progenitors based on the brightness of unresolved emission. We demonstrated that magnetic CVs – polars and intermediate polars – do not contribute more than ∼3 per cent to the observed CN frequency, assuming values of parameters most likely for the CN progenitors, the absolute upper limit being ≈10 per cent. We also showed that in dwarf novae $\gtrsim$90–95 per cent of the material is accreted during outbursts, and only a small fraction during quiescent periods.

ACKNOWLEDGMENTS

We thank the anonymous referee for useful comments. The authors are grateful to Hans Ritter for helpful discussions of cataclysmic variables. This research has made use of *Chandra* archival data provided by the *Chandra* X-ray Center. The publication makes use of software provided by the *Chandra* X-ray Center (CXC) in the application package CIAO. *XMM–Newton* is an ESA science mission with instruments and contributions directly funded by ESA Member States and the USA (National Aeronautics and Space Administration). The *Spitzer Space Telescope* is operated by the Jet Propulsion Laboratory, California Institute of Technology, under contract with the National Aeronautics and Space Administration.

REFERENCES

Araujo-Betancor S., Gänsicke B. T., Long K. S., Beuermann K., de Martino D., Sion E. M., Szkody P., 2005, ApJ, 622, 589
Arp H. C., 1956, AJ, 61, 15
Bogdán Á., Gilfanov M., 2008, MNRAS, 388, 56 (Paper I)
Brunschweiger J., Greiner J., Ajello M., Osborne J., 2009, A&A, 496, 121
Cannizzo J. K., Mattei J. A., 1992, ApJ, 401, 642
Csák B., Kiss L. L., Retter A., Jacob A., Kaspi S., 2005, A&A, 429, 599
Dickey J. M., Lockman F. J., 1990, ARA&A, 28, 215
Evans P. A., Hellier C., 2007, MNRAS, 663, 1277
Fujimoto M. Y., 1982, ApJ, 257, 752
Gilfanov M., 2004, MNRAS, 349, 146
Gilfanov M., Bogdan Á., 2010, Nat, 463, 924
Gordon K. D. et al., 2006, ApJ, 638, L87
Hamilton R. T., Urban J. A., Sion E. M., Riedel A. R., Voyer E. N., Marcy J. T., Lakatos S. L., 2007, ApJ, 667, 1139
Hickox R. C., Markevitch M., 2006, ApJ, 645, 95
Hoshi R., 1979, PThPh, 61, 1307
Irwin J. A., Athney A. E., Bregman J. N., 2003, ApJ, 587, 356
Jarrett T. H., Chester T., Cutri R., Schneider S. F., Huchra J. P., 2003, AJ, 125, 525
Kamath U. S., Anupama G. C., Ashok N. M., Chandrasekhar T., 1997, AJ, 114, 2671
Kennicutt R. C. Jr., 1998, ARA&A, 36, 189
King A. R., Lasota J. P., 1979, MNRAS, 188, 653
Kiss L. L., Gogh N., Vinkó J., Fűrész G., Csák B., DeBond H., Thomson J. R., Derekas A., 2002, A&A, 384, 982K
Koyama K., Hamaguchi K., Ueno S., Kobayashi N., Feigelson E. D., 1996, PASJ, 48, 87
Lamb D. Q., Masters A. R., 1979, ApJ, 234, 117
Landi R., Bassani L., Dean A. J., Bird A. J., Fiocchi M., Bazzano A., Nousek J. A., Osborne J. P., 2009, MNRAS, 392, 630
Li Z., Wang Q. D., 2007, ApJ, 668, 39L
Lipkin Y., Leibowitz E. M., Retter A., Shemmer O., 2001, MNRAS, 328, 1169
Macri L. M., 2001, ApJ, 549, 721
Moretti A., Campana S., Lazzati D., Tagliaferri G., 2003, ApJ, 588, 696
Mukai K., Kinkhabwala A., Peterson J. R., Kahn S. M., Paerels F., 2003, ApJ, 586, L77
Naik S., Banerjee D. P. K., Ashok N. M., 2009, MNRAS, 394, 1551
Nevalainen J., Markevitch M., Lumb D., 2005, ApJ, 629, 172
Nieten C., Neininger N., Guélin M., Ungerechts H., Lucas R., Berkhausen E. M., Beck R., Wielebinski R., 2006, A&A, 453, 459
Osaki Y., 1974, PASJ, 26, 429
Pandel D., Cordova F. A., Mason K. O., Priedhorsky W. C., 2005, ApJ, 626, 396
Panei J. A., Althaus L. G., Benvenuto O. G., 2000, A&A, 353, 970
Poggiani R., 2009, AN, 330, 77
Puebla R. E., Diaz M. P., Hubeny I., 2007, AJ, 134, 1923
Ramsay G., Cropper M., 2004, MNRAS, 347, 497
Revnivtsev M., Sazonov S., Gilfanov M., Churazov E., Sunyaev R., 2006, A&A, 452, 169
Revnivtsev M., Churazov E., Sazonov S., Forman W., Jones C., 2007, A&A, 473, 783
Ritter H., Kolb U., 2003, A&A, 404, 301
Sazonov S., Revnivtsev M., Gilfanov M., Churazov E., Sunyaev R., 2006, A&A, 450, 117
Shafter A. W., 1997, ApJ, 487, 226
Shafter A. W., Irby B. K., 2001, ApJ, 563, 767
Shtykovskiy P. E., Gilfanov M. R., 2007, AstL, 33, 437
Stanek K. Z., Garnavich P. M., 1998, ApJ, 503, 131
Starrfield S., Truran J. W., Sparks W. M., Kutter G. S., 1972, ApJ, 176, 169
Stockman H. S., Schmidt G. D., Lamb D. Q., 1988, ApJ, 332, 282
Strüder L. et al., 2001, A&A, 365, L18
Suleimanov V., Revnivtsev M., Ritter H., 2005, A&A, 435, 191
Townsley D. M., Bildsten L., 2004, ApJ, 600, 390
Trudolyubov S., Kotov O., Priedhorsky W., Cordova F., Mason K., 2005, ApJ, 634, 314
Turner M. J. L. et al., 2001, A&A, 365, L27
Urban J. A., Sion E. M., 2006, ApJ, 642, 1029
Vaytet N. M. H., O'Brien T. J., Rushton A. P., 2007, MNRAS, 380, 175
Voss R., Gilfanov M., 2007, A&A, 468, 49
Warner B., Woudt P. A., 2009, MNRAS, 397, 979
Williams S. J., Shafter A. W., 2004, ApJ, 612, 867
Wils P., Gänsicke B. T., Drake A. J., Southworth J., 2010, MNRAS, 402, 436
Yaron O., Prialnik D., Shara M. M., Kovetz A., 2005, ApJ, 623, 398

This paper has been typeset from a TEX/LATEX file prepared by the author.